

# Metamaterial based Printed Circuit Antenna for Blood Glucose Level Sensing Applications

Dhulfiqar Ali

Gaziantep University: Gaziantep Universitesi

Taha A. Elwi ([✉ taelwi82@gmail.com](mailto:taelwi82@gmail.com))

Al-Mammon University College <https://orcid.org/0000-0002-8389-5457>

Serkan Özbay

Gaziantep University: Gaziantep Universitesi

---

## Research Article

**Keywords:** Glucose, sensor, MTM, noninvasive

**Posted Date:** July 1st, 2021

**DOI:** <https://doi.org/10.21203/rs.3.rs-578165/v1>

**License:**  This work is licensed under a Creative Commons Attribution 4.0 International License.

[Read Full License](#)

---

# **Metamaterial based Printed Circuit Antenna for Blood Glucose Level Sensing Applications**

Dhulfiqar Ali<sup>1</sup>, Taha A. Elwi<sup>2</sup>, Serkan Özbay<sup>1</sup>

<sup>1</sup>Electrical Electronics Engineering Department, Gaziantep University

<sup>2</sup>Communication Engineering Department, Al-Mamoon University College

**Abstract**— Due to the urgent need to develop technologies for continuous glucose monitoring in diabetes individuals, a potential research has been applied by invoking the microwave techniques. Therefore, this work presents a novel technique based on a single port microwave circuit, antenna structure, based on Metamaterial (MTM) transmission line defected patch for sensing the blood glucose level in noninvasive process. For that, the proposed antenna is invoked to measure the blood glucose through the field leakages penetrated to the human blood through the skin. The proposed sensor is constructed from a closed loop connected to an interdigital capacitor to magnify the electric field fringing at the patch center. The proposed antenna sensor is found to operate excellently at the first mode, 0.6GHz, with  $S_{11}$  impedance matching less than -10dB. The proposed sensor performance is tested experimentally with 15 cases, different patients, through measuring the change in the  $S_{11}$  spectra after direct touching to the sensor a finger print of a patient. The proposed sensor is found to be effectively very efficient detector for blood glucose variation with a low manufacturing cost when printed on an FR-4 substrate. The experimental measurements are analyzed mathematically to obtain the calibration equation of the sensor from the curve fitting. Finally, the theoretical and the experimental results are found to be agreed very well with a percentage of error less than 10%.

**Key words:** Glucose, sensor, MTM, noninvasive.

## I. INTRODUCTION

Viktor Veselago first presented metamaterials (MTM) in 1967 [1]. Such structures may be called artificial materials with nontraditional properties [2]. These materials possess negative permittivity ( $\epsilon$ ) and negative permeability ( $\mu$ ) that in turn support the backward wave propagation of electromagnetic waves [3]. In 1999 an interesting subwavelength element realized as split ring resonator (SRR) to achieve negative permeability was proposed by Pendry [4]. Basically, SRR can be represented as tank of  $LC$  circuit possessing equivalent inductance ( $L$ ) and the capacitance ( $C$ ) between two concentric rings resonating at specific frequency [4]. The SRR has normally a size much less than, around wavelength ( $\lambda/10$ ), the guided wavelength. Therefore, many researchers applied SRR as technique to retrieve the characterizations of materials [4]. In such process, the changes in the scattering parameters (S-parameters) with respect to a sample under test (SUT) introduction can be transferred through certain algorithm to retrieve the materials characterizations.

Microwave sensing is a reliable method for liquid characterization that has been employed in the past decade [5]. SRRs [6], complementary SRRs (CSRRs) [3], open CSRRs (OCSRRs) [4], closed ring resonator [5] and other miniaturized microwave resonators [6] based on transmission lines attracted a considerable attention of researchers for biomedical applications [6]. The electromagnetic properties of these structures depend on their operation frequency and quality factor changes with respect to different liquid introductions [7]. Through measuring S-parameters coefficients, complex dielectric parameters of SUT, the liquid characterizations can be addressed [8]. This has provided a new sensing platform for the biological, pharmaceutical, and fuel industries [9]. Most microwave biological sensors are mounted under ultra-thin cylindrical pipes [10] or slotted cylindrical tubes [11]. Based on measuring S-parameters

magnitudes at certain frequency, materials under test losses can be extracted for quality detection [12]. Such technology, however, the resolution of high-losses was found a significant concern due to the issue of skin depth penetration [13]. On the other hand, most suggested methods require micro fluidic channel tubes to contain SUT; that add extra losses and difficulty of penetrations [14]. Nevertheless, many sensors detection process is based on certain volume of SUT that limits their use for real-time monitoring applications [15]. Moreover, an additional size and fabrication cost could be added to permeate the microwave reach to SUT [16]. In such technique, at certain liquid height such process is validated to ensure field retardation and phase change to analyze the dielectric characterization [17] in specific for biological solvent detection.

Based on the current development of microwave sensors technologies, fractal based MTM structures attracted researchers to realize effective and efficient sensors to achieve a high selectivity [18]. On top of that, MTM realizes excellent performance in the microwave ranges due to their nontraditional properties [19]. Moreover, MTM based fractal geometries use remain very excellent candidates in the biomedical aspects due to their size reduction in comparison to traditional microwave structures. For example, a MTM defected patch based monopole antenna was presented in [20] for pollution detections. Authors in [21] proposed a study of using a traditional microstrip transmission line for liquid properties detection. Then, an extended study based on a fractal MTM structure was presented for blood glucose sensing using a microstrip transmission line loaded with carbon nanotube patch in [22]. The use of MTM patch based nanoscale structures was introduced for gas detection in [23] and [24]. MTM based fractal structures were applied to realize as MTM defect on the ground plane for cancer cell detection based on their electrical properties changes [25].

Now, in this paper, a new approach based on a single port antenna element via MTM transmission line structure is proposed for blood glucose level detection. The MTM is constructed from an interdigital capacitor structure with a closed loop ring. The proposed structure is designed for glucose detection. The paper is organized as follows: The geometrical details are discussed in section II. The analysis process and the parametric study are presented in section III. The experimental measurements are explained in section IV after conducting 15 cases for the proposed study. The paper is concluded in section V.

## II. Sensor Design and Details

The proposed antenna is mounted on an FR-4 substrate of a dielectric constant  $\epsilon_r=4.3$  and loss tangent  $\tan\delta=0.025$  with thickness  $h=1.6$  mm. The copper metal is  $35\mu\text{m}$ . The proposed antenna is compacted on  $30\times30$  mm<sup>2</sup> size. The antenna is fed with a  $50\Omega$  microstrip transmission line of 7.25mm width and extended to touch the patch at length of 1.5mm to be connected directly to the radiating structure. The proposed closed loop design details are shown in Fig1(a). The back panel is covered completely copper as appeared in Fig1(b).

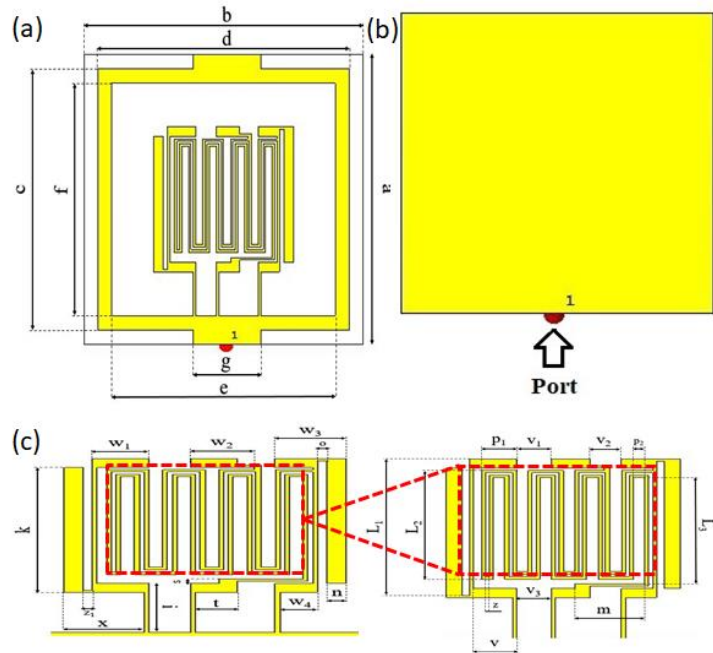


Fig1; Antenna design: (a) Front view, (b) Back view, and (c) Interdigital capacitor design.

In addition to the proposed closed loop in this design, a copper interdigital capacitor ( $C_{int}$ ), see Fig1(c), is conducted to maximize the electrical field intensity [12] at the center of the patch where SUT would be positioned. All geometrical details of Fig1 are listed in Table 1.

Table 1; Geometrical details of the proposed antenna sensor.

Parameter	Value (mm)	Parameter	Value (mm)
A	30	K	14
B	30	Z	0.25
C	27	Z1	0.5
D	27	I	5.5
E	24	S	0.5
F	24	N	1
G	7.25	V1	2.25
W1	3	V2	2
W2	2.5	V3	2.25
W3	3.75	V	2.75
W4	2	P1	2.25
O	0.5	P2	0.75
L1	14.75	T	2.25
L2	11.75	M	4.5
L3	11.5	X	4.25

### III. MTM Patch Theoretical Analysis

As mentioned later, the proposed radiating patch consists of a closed loop coupled with  $C_{int}$ . Therefore, the proposed patch is structured in such way to provide maximum fringing from the  $C_{int}$  edges. The  $C_{int}$  unit cell is constructed as interfaced strip lines with an effective length ( $L_n$ ) to provide the desirable resonant frequency ( $f_r$ ). The resulted capacitance value of the used  $C_{int}$  can be calculated analytically from the following equation [26]:

$$C = \frac{\varepsilon_{re} \times 10^{-3}}{18\pi} \frac{K(k)}{K'(k)} (n - 1) \frac{L}{10^{-6}} \quad (1)$$

where C is the capacitance in pF,  $\varepsilon_{re}$  is the effective relative permittivity, n is the capacitor figure number, L is the finger length, K and K' are elliptical integral coefficients and they are given as [27]:

$$K(k) = \int_0^{\frac{\pi}{2}} [1 - k \sin(t)^2]^{-0.5} dt \quad (2)$$

$$K'(k) = \int_0^{\frac{\pi}{2}} [1 - (\sqrt{1-k^2}) \sin(t)^2]^{-0.5} dt \quad (3)$$

where, k is the argument and can be calculated as [26]:

$$k = \left( \tan \left( \frac{a\pi}{4b} \right) \right)^2 \quad (4)$$

where:

$$a = \frac{W}{2} \text{ and } b = \frac{W+S}{2} \quad (5)$$

where, W is the finger width and S is the separation distance between fingers.

Now, the proposed sensor is analytically decomposed from the equivalent circuit diagram that is shown in Fig2. From Fig2, the proposed  $C_{int}$  is connected to two strip lines. The strip lines provide L-C branch ( $L_{strip}$  and  $C_{strip}$ ) connection in parallel with  $C_{int}$ . OCSSR structure is connected to  $C_{int}$  through three shoring posts to be presented by ( $L_{short}$ ) in the equivalent circuit diagram. It is good to mention that the effects of the inherent stray inductors ( $L_s$ ) and stray capacitors ( $C_s$ ) are proposed in the equivalent circuit diagram. Nevertheless, the feed line equivalently is considered as an inductor ( $L_{feed}$ ). The equivalent representation for the closed loop (CL) is considered as an inductor ( $L_{CL}$ ) and can be calculated according to the following equation [23]:

$$L = \mu_o a \left\{ \ln \left( \frac{8a}{Z_1} \right) - 2 \right\} \quad (6)$$

Based on the circuit model in Fig2, the authors calculated the relative lumped elements with an initial gauss from equations (1 and 6) for the proposed design at the desired frequency band using ADS software package parametrically. The S-parameters are calculated from the circuit model to be shown in Fig2. It is found that the proposed sensor shows a resonance mode at 0.63GHz according to the lumped elements that are listed in Table 2.

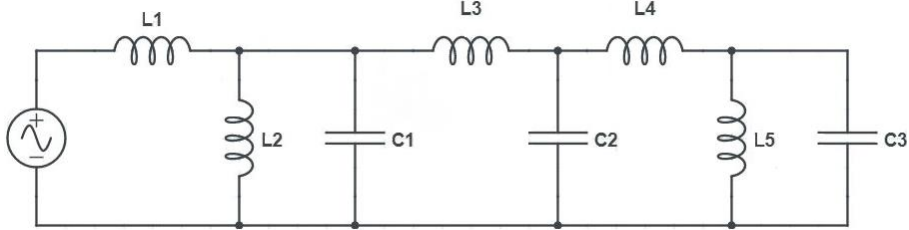


Fig2; Equivalent circuit for the proposed resonator.

Table 2; Calculated lumped elements of the equivalent circuit.

Lumped element	Value
L1	1.01nH
L2	1.89nH
L3	11.6mH
L4	23.04nH
L5	17.45nH
C1	11.12pF
C2	2.06pF
C3	1.91pF

From the proposed circuit model the equivalent impedance is calculated based on the second branch to be described by  $L_2$  and  $C_2$  be noted as  $Z_{T,2}$  following:

$$Z_{T,2} = \frac{j\omega L_2}{1 - \omega^2 L_2 C_2} \quad (7)$$

Therefore, the resonant frequency,  $f_{r,2}$  is expressed as

$$f_{r,2} = \frac{1}{2\pi\sqrt{L_2 C_2}}. \quad (8)$$

In Fig. 2, the equivalent circuit of the proposed patch can be represented as two series of  $L_1 C_c$  circuits and one parallel  $L_2 C_2$  circuit and the total impedance,  $Z_{T,1}$  in addition to the band pass resonant frequency,  $f_{r,1}$  which can be given as following:

$$Z_{T,1} = \frac{2(1 - \omega^2 L_1 C_c)}{j\omega C_c} + \frac{j\omega L_2}{1 - \omega^2 L_2 C_2}, \quad (9)$$

$$f_{r,1} = \frac{1}{2\pi\sqrt{L_1 C_c}}. \quad (10)$$

By employing (2) and (4), relation (3) can be rewritten as following:

$$Z_{T,1} = \frac{2(1 - (\frac{\omega}{\omega_{r,1}})^2)}{j\omega C_c} + \frac{j\omega L_2}{1 - (\frac{\omega}{\omega_{r,2}})^2} \quad (11)$$

$Z_{T,1}$  in relation (5) has two resonant frequencies, lower and upper frequencies which are represented by  $\omega_{r,1}$  and  $\omega_{r,2}$  respectively. When  $\omega = \omega_{r,1}$  a maximum transmission could occur, where minimum  $Z_{T,1}$  is ( $Z_{T,1} \geq j\omega L_2$ ), while zero transmission occurs at  $\omega = \omega_{r,2}$  where  $Z_{T,1}$  maximum is achieved. In order to confirm prior discussion, an electromagnetic 3D simulation based on CST software packages is invoked to validate the obtained results from the circuit model. In Fig3, the patch is simulated when mounted in closed to a transmission line to evaluate the  $S_{11}$  spectrum. It is found that there are three resonant frequencies,  $f_{r,1}$ ,  $f_{r,2}$  and  $f_{r,3}$ , all these frequencies are the same resonant frequencies of the proposed patch. Therefore, these frequencies can be used as indicators for characterizing SUT after applying sensitivity analysis at the resonant frequencies.

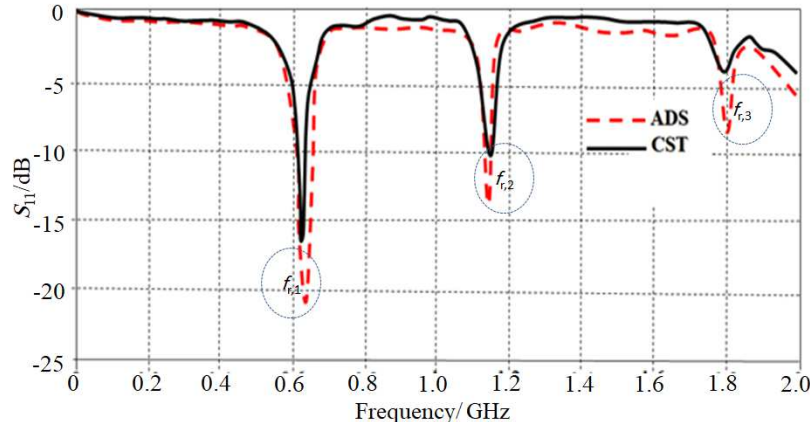


Fig 3;  $S_{11}$  spectra comparison between ADS and CST software packages.

#### IV. Sensitivity Analysis

The proposed sensor is invented based on a quasi-static small antenna [12] in which designed with an interdigital capacitor surrounded with closed loop. Due to such combination a current circulation occurs at three legs of connection between the capacitor and the closed loop. The

variation in the capacitance of the structure generally concerns on the variation in the permittivity of SUT. Therefore, the performance variation in the proposed structure with introducing different permittivity values is discussed as following:

### *1- Resonant frequencies analysis:*

After introducing different SUT in the CST MWS environment, the frequency shifts are recorded to be tested later experimentally. Therefore, SUT must cover the whole area for the efficient perturbation of the  $E$ -field. The resonant frequencies of  $S_{11}$  in Fig.4 are considered as the reference of unloaded filter ( $f_{r,1}$  and  $f_{r,2}$ ). The proposed sensor is then loaded with the SUT, where the dielectric constant of the sample is changed randomly in a broad range from 76 to 90. The resonant frequencies ( $f_{r,1}$  and  $f_{r,2}$ ) corresponding to each sample are extracted, which are also plotted with variation of the dielectric constant as shown in Fig. 4 (a). For preferable conception the change in the resonant frequencies ( $\Delta f_r = \text{unloaded } (f_{r,1} \text{ and } f_{r,2}) - \text{corresponding loaded } (f_{r,1} \text{ and } f_{r,2})$ ) is plotted in Fig. 4 (b).

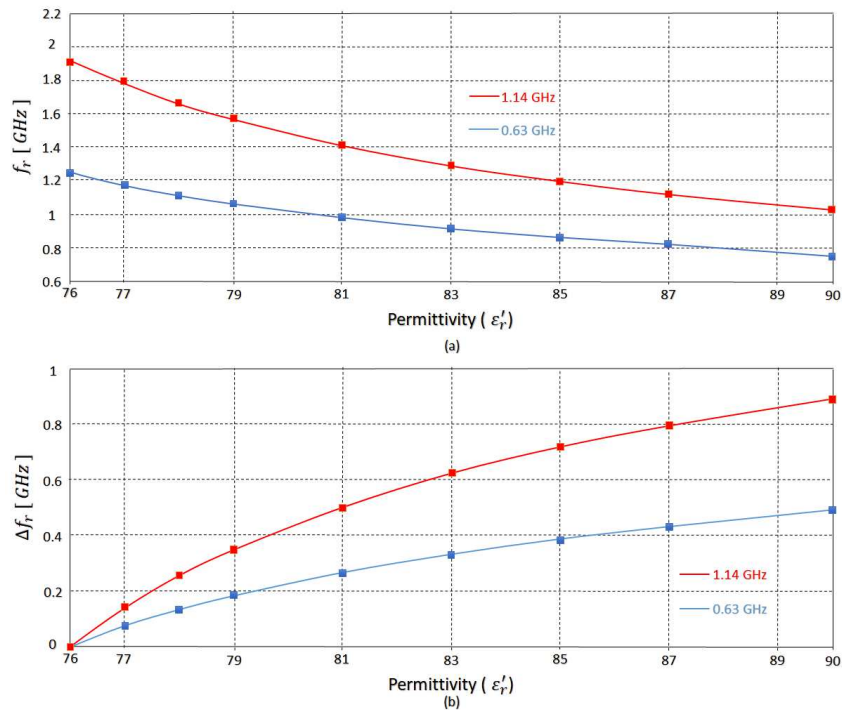


Fig. 4 Performance variation in terms of frequency resonance of the proposed sensor with changing  $\epsilon_r$ : (a)  $f_r$  change and (b)  $\Delta f_r^{-1}$ .

From Fig. 4 (a) it can be noted that the resonant frequency,  $f_{r,1}$  is about 170 MHz greater than resonant frequency,  $f_{r,2}$ . Moreover, the relative change  $f_{r,1}$  with dielectric constant is about 150 MHz greater than  $f_{r,2}$  as depicted in Fig. 4 (b). In another meaning, for these resonant frequencies,  $f_{r,1}$  shows to be a good preference to obtain high sensitivity for supposed dielectric constant as compared to that of resonant frequency,  $f_{r,1}$ .

## 2- Quality factor analysis:

For general resonators the quality factor,  $Q$  may be presented as [34]:

$$Q = \omega_0 \frac{W}{P_L} \quad (12)$$

where,  $\omega_0$  is the angular resonant frequency,  $W$  is the electric and magnetic stored energy and  $P_L$  represents the average power dissipated per cycle. The previous equation also can be rewritten as:

$$Q = \frac{f_r}{\Delta f} \quad (13)$$

where  $f_r$  is the resonant frequency and  $\Delta f$  represents the relative 3dB bandwidth of the resonator frequency response. The proposed sensor performance is simulated with different values of loss tangent from 0.01 to 0.15 and corresponding  $\epsilon'_r$  variation from 76 to 90. The relative quality factor is computed and depicted in Fig. 5.

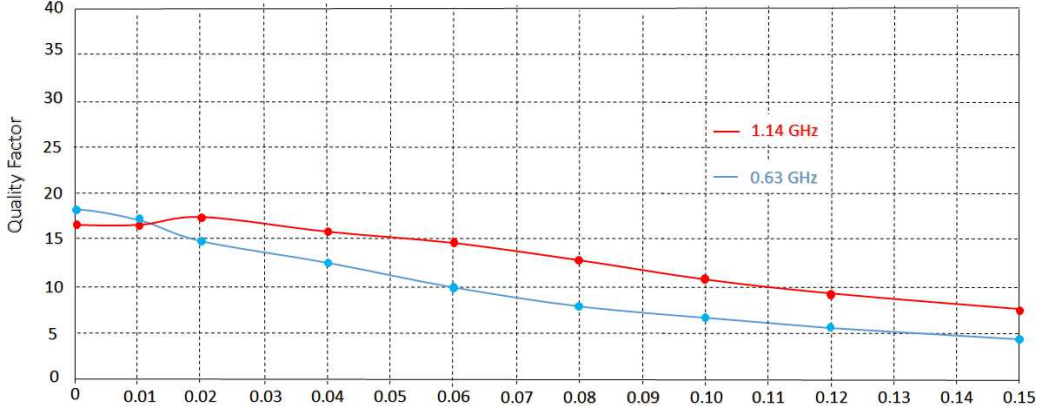


Fig. 5; Quality factor variation of the proposed sensor calculated for  $f_{r,1}$  and  $f_{r,2}$ .

From Fig. 5, it is fully interesting to observe that the slope of quality factor is identical to resonant  $f_{r,1}$  in comparison to  $f_{r,2}$  slope with loss tangent change. While the slope of quality factor relative to  $f_{r,1}$  is greater than in  $f_{r,2}$  for the same condition. Hence the resonant  $f_{r,1}$  is utilized for characterizing the SUT.

## V. Curve Fitting Analysis and Calibration Equations

Now, the obtained results from the previous section are analyzed to evaluate the calibration sensitivity to be compared to the experimental results. In order to describe the tested samples, a numerical type is desired which generally plots the measured parameters (e.g., the resonant frequency and the quality factor) to the relative permittivity of the SUT.

### 1- Real permittivity calibration effects

The proposed sensor frequency resonance is found to be changed due to samples loading as can be observed in Fig.6; in which the inverse square of the resonant frequency ( $f_r$ ) is extracted from the  $S_{11}$  spectra. The results with the corresponding real permittivity ( $\epsilon'_r$ ) of SUT are depicted in Fig. 6.

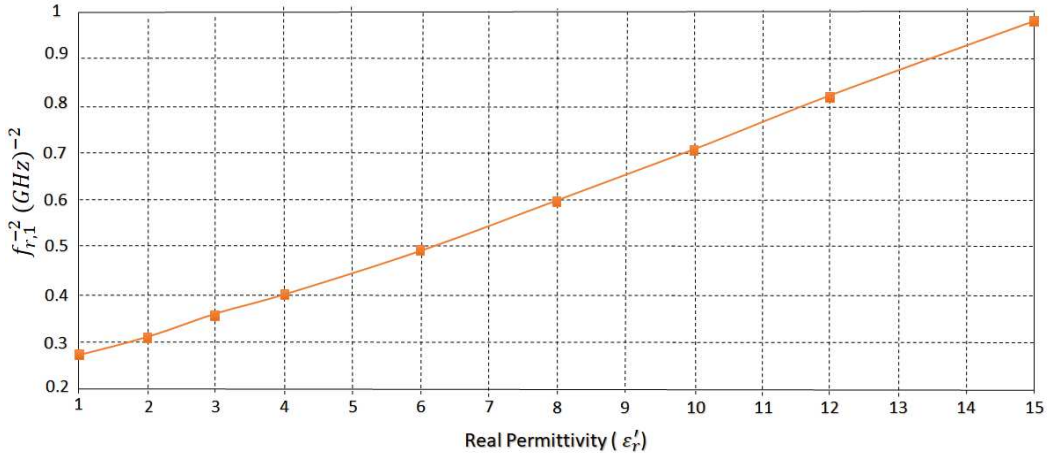


Fig. 6.  $f_{r,1}^{-2}$  variation with respect of changing  $\epsilon'_r$ .

The obtained results in Fig. 6 confirm the results in equation (10) that is achieved from the equivalent circuit model. From equation (10), the values of  $L_2$  and  $C_2$  are supposed to be constant due to the solid values of the overall length of OCSRRs and  $\epsilon_r$  of the substrate. It is interesting to note that the inverse square of the resonant frequency is directly proportional to the real permittivity of the SUT. Thus, in order to combine all the above effects, the dielectric constant of the SUT is mathematically expressed in terms of the resonant frequency ( $f_r$ ) as following:

$$\epsilon'_r = -3.519(f_r^{-2})^2 + 23.84(f_r^{-2}) - 5.007 \quad (14)$$

The above relation is obtained from employing the curve fitting tools, which supplies a numerical model of the proposed sensor to determine the real permittivity of SUT in terms of the measured resonant frequency ( $f_{r,1}$ ). It should be noted that all SUT has with a fixed 3mm thickness.

## 2- Imaginary permittivity calibration effects

After founding the numerical relations to determine the dielectric constant of SUT, an identical analysis is completed to find a numerical relation for computing the loss tangent ( $\tan\delta$ ) of SUT. As explained earlier that the resonant  $f_{r,1}$  provides a quality factor greater than those obtained at  $f_{r,2}$ . Hence, the resonant  $f_{r,1}$  is employed for calculating  $\tan\delta$  of SUT. Therefore, at

first, the dielectric constant in the range of 76 to 90 are possessed and the  $\tan\delta$  values combatable for each dielectric SUT is changed from 0 to 0.15, and the relative simulated results of  $f_{r,1}$  change is depicted in Fig. 7. The quality factor ( $Q_{SUT}$ ) for each case is determined from the simulated response of  $S_{11}$ spectra, after that the inverse of  $Q_{SUT}$  values and the corresponding  $\tan\delta$  are depicted in Fig. 7. The relation between the  $\tan\delta$  and the  $Q_{SUT}$  can be specified as following [12]:

$$Q_{MUT} = \frac{1}{\tan\delta} = \frac{\epsilon_r''}{\epsilon_r'} \quad (15)$$

where  $\epsilon_r'$  and  $\epsilon_r''$  are the real and imaginary parts of the relative permittivity in equation (15).

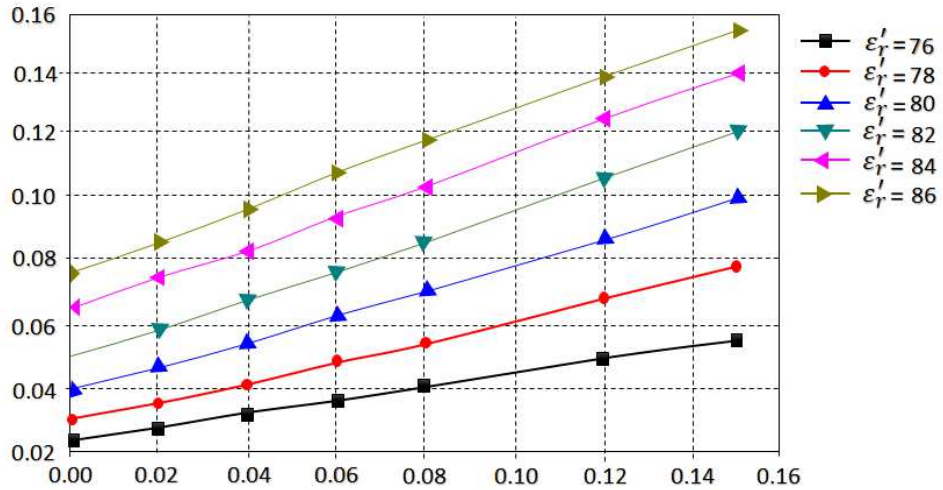


Fig. 7. Inverse of Q-factor in terms of  $\tan\delta$  for various values of  $\epsilon'_r$  (Linear relevance between  $Q_{SUT}^{-1}$  and  $\tan\delta$  for all values of  $\epsilon'_r$ )

From Fig. 7, it is noted that the alteration of  $Q_{SUT}^{-1}$  with  $\tan\delta$  is linear compound with a rising values depend on  $\epsilon'_r$  of SUT. Thus, to deduce the  $\tan\delta$  of SUT, which relies on the loaded quality factor as well as the  $\epsilon'_r$  of SUT, a curve fitting tool is utilized to conclude the numerical model as presented below:

$$\tan\delta = \exp\left(\frac{Q_{MUT}^{-1} + 0.02393}{0.2183 + 0.03131 \times \epsilon_r}\right) - 1.16477 \quad (16)$$

After deciding the  $\epsilon'_r$  from equation (14) and  $\tan\delta$  from (16), the imaginary part of the complex permittivity can be determined using (15).

## VI. Sensor Performance and Measurements

The proposed sensor is fabricated using printed circuit board technology as shown in Fig. 9. The sensor is fabricated from using chemical wet etching process in the laboratory. The FR4 substrate is considered as the plate form layer for the proposed sensor.

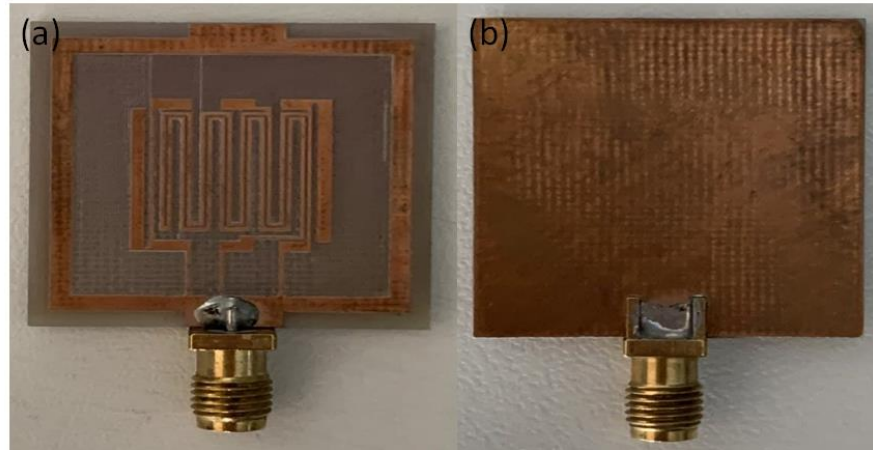


Fig. 8; Fabricated sensor structure: (a) front view and (b) back view.

Now, the proposed sensor performance is measured in terms of  $S_{11}$  spectrum as seen in Fig. 10 without introducing any SUT. The obtained results from measurements are compared to those obtained from simulation results to show excellent agreement as seen in Fig.9. The measurement results are conducted to PNA8720 network analyzer after applying a single port calibration process. From the measured  $S_{11}$  spectra, the proposed sensor shows a frequency resonance at 0.63 GHz with  $|S_{11}|=16\text{dB}$ , and a bandwidth from 0.6GHz to 0.65GHz. This frequency is considered to ensure excellent penetration through the human tissues with minimum skin depth loss [6].

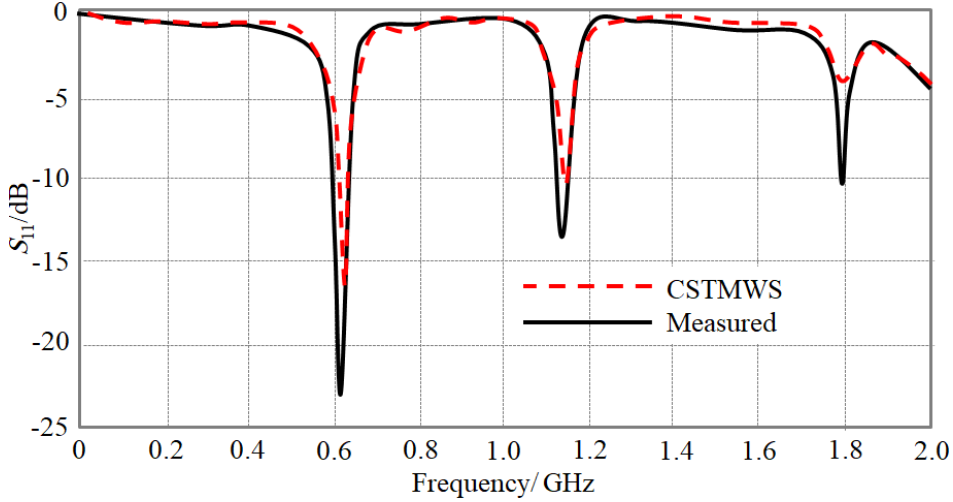


Fig 9; Experimental validation.

## VII. Sensing Measurements and Validations

In this section, the proposed sensor measurement operation is based on placing a finger on the interdigital capacitor part to monitor the variation in the  $S_{11}$  magnitude and frequency resonance shift. The field penetration through the finger skin is affected by the blood glucose variation [12]. Such variation is attributed to the blood glucose change that could be reflected on the effective permittivity of the blood as discussed [23]. Therefore, the effects of touching the proposed sensor by 15 patients at three different times to realize 45 recorders are listed in Table 3 to analyze the sensor performance. The recorded data in Table 3 are collected based on  $S_{11}$  spectra change in terms of  $S_{11}$  magnitude, frequency resonance, phase change, bandwidth, and quality factor.

### *1- Sensing Process*

The  $S_{11}$  spectra of the proposed sensor are obtained according to the samples listed in Table 3. The sensor is designed to ensure that the first resonant position is located around 0.63 GHz. Therefore, the fabricated sensor  $S_{11}$  spectra changes are evaluated after introducing the patient finger touch. Thus, the prepared design is experimentally tested using the PNA8720

network analyzer. The obtained changes in the  $S_{11}$  spectra are monitored in terms of  $|S_{11}|$ , frequency shift, phase change, quality factor, and bandwidth.

Table 3; Clarification of the results of measuring different blood samples

Case number	BMI	Age/year	Sex	Glucose level	$f_{r,1}$ shift/GHz	$Q_{SUT}/\%$	$\epsilon_r'$	$\epsilon_r''$
1	18.9	8	M	112	0.1091	12	25.91	0.311
				210	0.112	11	25.76	0.283
				150	0.115	11	25.59	0.281
2	23.1	49	M	119	0.106	12	26.08	0.313
				103	0.115	15	25.59	0.3833
				210	0.111	22	25.81	0.567
3	22.9	65	F	250	0.123	9	25.16	0.226
				225	0.193	8	21.59	0.172
				245	0.191	21	21.69	0.455
4	27.8	50	F	131	0.103	31	26.25	0.813
				159	0.109	9	25.92	0.233
				177	0.108	12	25.97	0.311
5	26.5	59	F	331	0.121	11	25.27	0.278
				193	0.111	13	25.81	0.335
				168	0.156	17	23.43	0.398
6	29.9	38	F	102	0.116	15	25.54	0.383
				131	0.182	10	22.13	0.221
				109	0.174	9	22.52	0.202
7	30.2	44	M	158	0.091	16	26.9	0.43
				146	0.098	13	26.52	0.344
				126	0.092	10	26.85	0.268
8	28.5	43	M	110	0.109	11	25.92	0.282
				191	0.106	12	26.08	0.313
				198	0.110	11	25.87	0.284
9	24.1	48	F	104	0.122	7	25.22	0.176
				107	0.133	7	24.63	0.172
				115	0.124	9	25.11	0.226
10	32.6	41	F	119	0.111	11	25.81	0.283
				131	0.110	13	25.87	0.336
				114	0.113	12	25.7	0.308
11	36.1	53	M	121	0.091	10	26.9	0.269
				180	0.094	7	26.74	0.187
				140	0.092	11	26.85	0.295
12	32.6	67	F	390	0.109	9	25.92	0.233
				331	0.101	7	26.36	0.184
				378	0.105	12	26.14	0.313
13	22.4	61	F	190	0.189	11	21.79	0.239
				143	0.188	10	21.83	0.218
				126	0.177	9	22.37	0.201
14	23.5	62	M	129	0.109	12	25.92	0.311
				130	0.110	11	25.87	0.284
				120	0.112	9	25.76	0.231
15	24.9	54	M	121	0.195	4	21.5	0.086
				189	0.196	5	21.45	0.107
				134	0.179	8	22.28	0.178

## 2- Sensing Validation

The variation in the  $S_{11}$  spectra of the proposed sensor is measured after placing a finger on it as a non-invasive technique. Therefore, the glucose level is monitored through a normal device glucose meter, PRODIGY Autocode, and the results are recorded in Table 3. Then, the patient finger is placed on the proposed sensor and the frequency resonance shift and  $S_{11}$  magnitude change are listed in Table 3.

Next, the measured glucose level is compared with respect to the relative values of  $\epsilon_r'$  and  $\epsilon_r''$  that are listed in Table 3. Therefore, the measured  $f_{r,1}$  and  $Q_{SUT}$  values are applied in equation (14) to (15) to calculate the relative values of  $\epsilon_r'$  and  $\epsilon_r''$  from the measured data. The calculated values of  $\epsilon_r'$  and  $\epsilon_r''$  are compared to their relatives from measurements in Table 3. Thus, in Table 4, the relative errors between the measured and calculated  $\epsilon_r'$  and  $\epsilon_r''$  values are calculated. It is found a good agreement between the measured and calculated values. Therefore, from this comparison between the relative values of  $\epsilon_r'$  and  $\epsilon_r''$ , the glucose level can be detected according to Table 4.

Table 4; Comparison relative errors between the measured and calculated  $\epsilon_r'$  and  $\epsilon_r''$  values

Case number	Measured values		Calculated values		Error rate for $\epsilon_r'$	Error rate for $\epsilon_r''$	Total error rate
	$\epsilon_r'$	$\epsilon_r''$	$\epsilon_r'$	$\epsilon_r''$			
1	25.91	0.311	26.84	0.322	3.46%	3.41%	6.87%
	25.76	0.283	25.87	0.284	0.42%	0.35%	0.77%
	25.59	0.281	26.52	0.291	3.5%	3.43%	6.93%
2	26.08	0.313	27.01	0.324	3.44%	3.39%	6.83%
	25.59	0.383	26.52	0.397	3.5%	3.52%	7.02%
	25.81	0.567	26.73	0.588	3.44%	3.57%	7.02%
3	25.16	0.226	26.09	0.234	3.56%	3.41%	6.97%
	21.59	0.172	22.51	0.180	4.08%	4.44%	8.52%
	21.69	0.455	22.61	0.474	4.06%	4%	8.06%

4	26.25	0.813	27.17	0.842	3.38%	3.44%	6.82%
	25.92	0.233	26.84	0.241	3.42%	3.31%	6.73%
	25.97	0.311	26.90	0.322	3.45%	3.41%	6.86%
5	25.27	0.278	26.19	0.288	3.51%	3.47%	6.98%
	25.81	0.335	26.73	0.347	3.44%	3.45%	6.89%
	23.43	0.398	24.36	0.414	3.81%	3.86%	7.67%
6	25.54	0.383	26.46	0.396	3.47%	3.28%	6.75%
	22.13	0.221	23.05	0.230	3.99%	3.91%	7.90%
	22.52	0.202	23.45	0.211	3.96%	4.26%	8.22%
7	26.9	0.43	27.83	0.445	3.34%	3.37%	6.71%
	26.52	0.344	27.44	0.356	3.35%	3.37%	6.72%
	26.85	0.268	27.77	0.277	3.31%	3.24%	6.55%
8	25.92	0.285	26.84	0.295	3.46%	3.38%	6.84%
	26.08	0.313	27.01	0.324	3.44%	3.39%	6.83%
	25.87	0.284	26.79	0.182	3.43%	56.04%	59.47%
9	25.22	0.176	26.14	0.230	3.51%	23.47%	26.98%
	24.63	0.172	25.56	0.234	3.63%	26.49%	30.12%
	25.11	0.226	26.03	0.294	3.53%	23.12%	26.65%
10	25.81	0.283	26.73	0.348	3.44%	18.67%	22.11%
	25.87	0.336	26.79	0.319	3.43%	5.32%	8.75%
	25.7	0.308	26.63	0.319	3.49%	3.44%	6.93%
11	26.9	0.269	27.83	0.278	3.34%	3.23%	6.57%
	26.74	0.187	27.66	0.193	3.32%	3.26%	6.58%
	26.85	0.295	27.77	0.305	3.31%	3.27%	6.58%
12	25.92	0.233	26.84	0.241	3.42%	3.31%	6.73%
	26.36	0.184	27.28	0.190	3.37%	3.15%	6.52%
	26.14	0.313	27.06	0.324	3.39%	3.39%	6.78%
13	21.79	0.239	22.71	0.249	4.05%	4.01%	8.06%
	21.83	0.218	22.76	0.227	4.08%	3.96%	8.04%

	22.37	0.201	23.30	0.209	3.99%	3.77%	7.76%
14	25.92	0.311	26.84	0.322	3.42%	3.41%	6.83%
	25.87	0.284	26.79	0.294	3.25%	3.40%	6.65%
	25.76	0.231	25.82	0.232	0.23%	0.43%	0.66%
15	21.5	0.086	22.42	0.089	4.23%	3.37%	7.60%
	21.45	0.107	22.37	0.111	4.11%	3.60%	7.71%
	22.28	0.178	23.20	0.185	3.96%	3.78%	7.74%
					Total error ratio for all measurements	9.76%	

The total calculated error is evaluated from Table 4 according to the following equation:

$$\text{*error} = \frac{\| \text{measured values} - \text{calculated values} \|}{\text{calculated values}} \times 100\% \quad (17)$$

It is found the maximum error from the total values is less than 10%.

### VIII. Conclusion

The proposed sensor is presented to characterize blood glucose level through measuring the relative values of  $\epsilon_r'$  and  $\epsilon_r''$  for different blood samples. The proposed sensor is constructed as a single-port network; therefore, it is designed based on an interdigital capacitor patch to sense the blood glucose level non-invasively. The reason of that, the field fringing from the proposed sensor is found to be magnified and easy to penetrate through the human skin to the blood vassals. It is found that the proposed sensor shows different frequency resonances within the band of interest. However, it is decided to consider only the first frequency resonance ( $f_{r,1}$ ) for sensing where the maximum sensitivity can be achieved. In this case,  $f_{r,1}$  and  $Q_{SUT}$  measurement are gathered from different patients. Therefore, from the measured values, an analytical model is synthesized based on curve fitting analysis. In such process, fifteen patients are submitted to the proposed sensor for estimating the level of glucose in the blood, ending with results very similar

to the results measured by traditional commercial methods. The measured values of  $\varepsilon_r'$  and  $\varepsilon_r''$  are found to be agree very well with those obtained from the calculated results based on curve fitting analysis with less than 15% errors. It is found that the proposed sensor is a suitable choice for biomedical applications including blood glucose measurements. Finally, the proposed measurements point out the total error is about 10%.

### **Declarations**

We confirm here that the following sections are

\*Funding: 'Not applicable'

\*Conflicts of interest: 'Not applicable'

\*Availability of data and material: 'Not applicable'

\*Code availability (software application or custom code)

\*Authors' contributions: 'Not applicable'

### **References**

1. Whiting, D., Guariguata, L., Weil, C. & Shaw, J. IDF diabetes atlas: global estimates of the prevalence of diabetes for 2011 and 2030. *Diabetes Res. Clin. Pract.* 94(3), 311–321 (2011).
2. WHO. WHO\_World Health Day 2016\_WHO Calls for Global Action to Halt Rise in and Improve Care for People with Diabetes. Technical Report (2016).
3. American Diabetes Association. Diagnosis and classification of diabetes mellitus. *Diabetes Care* 37, S81–S90 (2014).

4. Bansal, N. Pre diabetes diagnosis and treatment: a review. *World J. Diabetes* 6(2), 296–303 (2015).
5. Burt, M. G., Roberts, G. W., Aguilar-Loza, N. R. & Stranks, S. N. Brief report: comparison of continuous glucose monitoring and finger-prick blood glucose levels in hospitalized patients administered basal-bolus insulin. *Diabetes Technol. Ter.* 15(3), 241–245 (2013).
6. Gonzales, W. V., Mobashsher, A. T. & Abbosh, A. Te progress of glucose monitoring—a review of invasive to minimally and non-invasive techniques, devices and sensors. *Sensors* 19(4), 800 (2019).
7. Lin, T., Gal, A., Mayzel, Y., Horman, K. & Bahartan, K. Non-invasive glucose monitoring: a review of challenges and recent advances. *Curr. Trends Biomed. Eng. Biosci.* 6(5), 1–8 (2017).
8. Spegazzini, N. et al. Spectroscopic approach for dynamic bioanalyte tracking with minimal concentration information. *Sci. Rep.* 4, 7013 (2015).
9. Kuroda, M. et al. Efcts of daily glucose fluctuations on the healing response to everolimus-eluting stent implantation as assessed using continuous glucose monitoring and optical coherence tomography. *Cardiovasc. Diabetol.* 15(1), 79 (2016).
10. Sim, J. Y., Ahn, C. G., Jeong, E. J. & Kim, B. K. In vivo microscopic photoacoustic spectroscopy for non-invasive glucose monitoring invulnerable to skin secretion products. *Sci. Rep.* 8(1), 1059 (2018).
11. Goodarzi, M. & Saeys, W. Selection of the most informative near infrared spectroscopy wavebands for continuous glucose monitoring in human serum. *Talanta* 146, 155–165 (2016).

12. Yadav, J., Rani, A., Singh, V. & Murari, B. M. Prospects and limitations of non-invasive blood glucose monitoring using near infrared spectroscopy. *Biomed. Signal Process. Control* 18, 214–227 (2015).
13. Vashist, S. K. Non-invasive glucose monitoring technology in diabetes management: a review. *Anal. Chim. Acta* 750, 16–27 (2012).
14. Sempionatto, J. R. et al. Eyeglasses-based tear biosensing system: Non-invasive detection of alcohol, vitamins and glucose. *Biosens. Bioelectron.* 137, 161–170 (2019).
15. Chen, L. et al. Cellular wireless energy harvesting for smart contact lens applications [Education corner]. *IEEE Antennas Propag. Mag.* 60(5), 108–124 (2018).
16. Zhang, J. et al. Noninvasive diagnostic devices for diabetes through measuring tear glucose. *J. Diabetes Sci. Technol.* 5(1), 166–172 (2011).
17. De Castro, L. F. et al. Salivary diagnostics on paper microfluidic devices and their use as wearable sensors for glucose monitoring. *Anal. Bioanal. Chem.* 411(19), 4919–4928 (2019).
18. Karpova, E. V. et al. Noninvasive diabetes monitoring through continuous analysis of sweat using fow-through glucose biosensor. *Anal. Chem.* 91(6), 3778–3783 (2019).
19. Bariya, M., Nyein, H. Y. Y. & Javey, A. Wearable sweat sensors. *Nat. Electron.* 1(3), 160–171 (2018).
20. Karyakin, A. A. et al. Non-invasive monitoring of diabetes through analysis of the exhaled breath condensate (aerosol). *Electrochim. Commun.* 83, 81–84 (2017).
21. Lipani, L. et al. Non-invasive, transdermal, path-selective and specific glucose monitoring via a graphene-based platform. *Nat. Nanotechnol.* 13(6), 504–511 (2018).

22. Kim, J., Campbell, A. S. & Wang, J. Wearable non-invasive epidermal glucose sensors: a review. *Talanta* 177, 163–170 (2018).
23. Segman, Y. Device and method for noninvasive glucose assessment. *J. Diabetes Sci. Technol.* 12(6), 1159–1168 (2018).
24. Amir, O. et al. Continuous noninvasive glucose monitoring technology based on “occlusion spectroscopy”. *J. Diabetes Sci. Technol.* 1(4), 463–469 (2007).
25. World Global Network. Helo Extense. <https://website.worldgn.com/heloextense/>. Accessed 15 June 2020.
26. Harman-Boehm, I. et al. Noninvasive glucose monitoring: increasing accuracy by combination of multi-technology and multisensors. *J. Diabetes Sci. Technol.* 4(3), 583–595 (2010).
27. Saha, S. et al. A glucose sensing system based on transmission measurements at millimetre waves using micro strip patch antennas. *Sci. Rep.* 7, 6855 (2017).